Supporting Information

Sekhar et al. 10.1073/pnas.1601846113

SI Text

Methodology.

Pulse sequence. The pulse scheme for measuring PREs in conformationally excited protein states is shown in Fig. 2*A*. The approach is based on amide ^{1}H CEST in which a series of ^{1}H-^{15}N HSQC spectra is recorded as a function of the position of a weak ^{1}H B_1 field (typically 15–50 Hz) that leads to a perturbation (in some cases saturation) of amide proton magnetization derived from spins in ground and excited states of interconverting conformers. In the scheme of Fig. 2*A*, narrow and wide filled bars represent 90° and 180° pulses, respectively, that are applied with phase x, unless specifically noted otherwise. Open shapes correspond to water selective 90° pulses and are applied with either rectangular or SEDUCE 1 profiles (59). Striped 180° pulses are of the composite variety, 90°$_x$-180°$_y$-90°$_x$ (57). The delay τ_a is set to 2.72 ms, and the phase cycle is ϕ_1 = (x,–x), receiver = (x,–x). Gradient strengths for g1, g2, g3, g5, g6, and g7 are 16, –20, 24, –16, –36, and 40 G/cm, respectively, and durations are 1, 0.4, 1, 1.2, 0.6, and 0.4 ms. Gradient g4 is applied at a strength of 0.1 G/cm for the t_1 period.

Consider a two-state exchanging system, $G \underset{k_{EG}}{\overset{k_{GE}}{\rightleftharpoons}} E$, as in the case of the hTRF1 protein studied here, with $k_{GE} << k_{EG}$, so that $p_E << p_G$, and where G and E are the ground and excited states (main text). The flow of magnetization during the pulse sequence can be summarized succinctly as follows:

$$\begin{aligned} H_z^G &\xrightarrow{J_{NH}} 2H_z^G N_x^G \xrightarrow{t_1} 2H_z^G N_x^G(\omega_N^G) \rightarrow 2H_z^G N_z^G(\omega_N^G) \\ &\xrightarrow{T_{EX}} \alpha(\omega_{CEST}) 2H_z^G N_z^G(\omega_N^G) \rightarrow \alpha(\omega_{CEST}) H_x^G(\omega_N^G) \\ &\xrightarrow{t_2} \alpha(\omega_{CEST}) H_x^G(\omega_N^G, \omega_H^G), \end{aligned} \quad \text{[S1]}$$

where A_i^j are A ε (^{1}H,^{15}N) i ε (x,y,z) magnetization components of state j ε (G,E), and the arrows denote magnetization transfer steps due to scalar couplings (J_{NH}) or evolution (chemical shift) during t_1, t_2 or spin relaxation (during T_{EX}). Briefly, ^{1}H magnetization of the ground state is converted to antiphase transverse nitrogen magnetization via an INEPT module (60) with ^{15}N chemical shifts subsequently recorded (denoted by ω_N^G in Eq. **S1**). During the following mixing period of duration T_{EX} a weak ^{1}H B_1 field is applied at a ^{1}H frequency within the amide ^{1}H chemical shift range (one ^{1}H-^{15}N plane collected for each frequency). When the frequency of the weak B_1 field is not coincident with either resonance frequencies of spins in ground and excited states (that is, $\omega_{CEST} \neq \omega_H^G, \neq \omega_H^E$), then $\alpha = \exp(-R_{2HzNz} T_{EX})$ and the T_{EX} element simply leads to signal attenuation due to relaxation during this delay. In contrast, when $\omega_{CEST} = \omega_H^G$ or $\omega_{CEST} = \omega_H^E$, then $\alpha \ll \exp(-R_{2HzNz} T_{EX})$ because of either a saturation effect ($\omega_{CEST} = \omega_H^G$) or a transfer of the perturbation from the excited state to the ground state through chemical exchange ($\omega_{CEST} = \omega_H^E$). Note that ^{15}N decoupling is not applied during T_{EX}, because even small levels of ^{15}N B_1 inhomogeneity lead to significant losses in signal due to attenuation of longitudinal order. As a result, major and minor dips of ^{1}H CEST profiles are split into doublets, separated by J_{NH} Hz, although with the sizes of the B_1 fields typically used the couplings are often not resolved.

Data acquisition. ^{1}H CEST measurements were carried out on samples of 800 μM ^{2}H/^{15}N K52C-tempol hTRF1, where the spin label is either reduced or oxidized, as well as a twofold diluted oxidized sample. T_{EX} was set to 125 ms in all cases. For both concentrated samples, data were acquired at four B_1 field strengths, 16, 26, 37, and 53 Hz, varying the irradiation frequency from 6.3 to 9.7 ppm in steps of 25, 30, 40, and 50 Hz, respectively, with each dataset comprised of 83, 69, 52, and 42 planes. ^{1}H CEST datasets recorded with a pair of B_1 fields, 26 and 53 Hz, were collected for the 400 μM oxidized sample, with the B_1 field spaced 30 (69 planes) and 50 (42 planes) Hz apart, respectively. As in our previous implementations of CEST (18), each dataset (corresponding to a single B_1 field) additionally contained a reference plane for which T_{EX} is set to 0 s.

It is worth noting that we observed some reduction of the spin label during the course of the four CEST experiments (four B_1 fields) when they were recorded over a period of 2 d (increases in CEST baselines over time). As a result, all datasets were acquired in 1 d using two scans per FID. Under these conditions, the spin label remained fully oxidized, with no changes in baselines from one dataset to the next.

Calibrating the CEST B_1 field. CEST B_1 fields were calibrated as described earlier (18) with a number of small modifications. Because J_{NH} evolution is active during the T_{EX} period, B_1 calibration is done by following the intensity of one of the doublet components in 1D ^{1}H spectra that are recorded in the absence of ^{15}N decoupling during acquisition (sequence of Fig. 2*A*). Note that there is a single ^{15}N 180° pulse between the T_{EX} period and the acquisition time (t_2), leading to the interconversion of the doublet components. Thus, if the calibration is carried out by irradiating the downfield (anti-TROSY) component, the intensity modulation will appear on the upfield (TROSY) component and vice versa.

Although CEST-derived chemical shifts of the excited state are extremely robust to experimental error, CEST-derived R_2 values are sensitive to errors in B_1 calibration. We quantified the expected errors in R_2 from B_1 miscalibration via a set of simulations as detailed below with one realization of random noise, whereby CEST profiles have been fit with the correct B_1 value (as used in the simulations) or with misset values that are either higher (by 3% or 6%) or lower (3%, 6%) than the actual field. Ground and excited state R_2 values from the fit, R_2^G and R_2^E respectively, were then correlated to the values obtained using the correct B_1 (Fig. S7). Results from these simulations show that for the range of R_2 rates in the present application, errors on the order of ±4 and ±10 s^{-1} are obtained when B_1 values are incorrect by 3% and 6%, respectively, with larger (smaller) B_1 values leading to under-(over-) estimates in extracted rates. To minimize errors in B_1 values, we used an approach whereby fields were calibrated for five different values ranging between 25 and 125 Hz and the resulting input vs. output B_1 field estimated from a linear fit of the data. Calibrations using different peaks were usually consistent within 2%. It is noteworthy that when fields on the order of 15 Hz were calibrated directly and were not estimated based on extrapolation from the calibration curve, significantly (≥1.5-fold) higher χ^2_{red} values were obtained from global data fits.

Extracting intensities and fitting ^{1}H CEST profiles. Cross-peak intensities in CEST datasets (I, $T_{EX} \neq 0$; I_o, $T_{EX} = 0$) were quantified from fits of peak lineshapes using the program FuDA (pound.med.utoronto.ca/~flemming/fuda/), as described previously (18). CEST profiles were constructed as the ratio I/I_o as a function of the irradiation frequency.

Twenty residues with distinct major and minor dips ($|\Delta\varpi_{GE}|$ > ~0.3 ppm) were fit globally to a two-state exchange model using the program Chemex (https://github.com/gbouvignies/chemex), which numerically propagates the Bloch–McConnell equation as described in Bouvignies and Kay (33).

$$\frac{d\vec{M}(t)}{dt} = \tilde{L}\vec{M}(t) \qquad \textbf{[S2]}$$

In Eq. **S2**

$$\vec{M} = \left[H_x^G \quad H_y^G \quad H_z^G \quad 2H_x^G N_z^G \quad 2H_y^G N_z^G \quad 2H_z^G N_z^G \quad H_x^E \quad H_y^E \quad H_z^E \quad 2H_x^E N_z^E \quad 2H_y^E N_z^E \quad 2H_z^E N_z^E \right]^T,$$

is a column vector containing the relevant basis operators (T is transpose) and

$$\tilde{L} = \begin{bmatrix} \tilde{R}_G^{6\times6} & \tilde{0}_6 \\ \tilde{0}_6 & \tilde{R}_E^{6\times6} \end{bmatrix} + \begin{bmatrix} -k_{GE} & k_{EG} \\ k_{GE} & -k_{EG} \end{bmatrix} \otimes \tilde{1}_6, \qquad \textbf{[S3]}$$

where $\tilde{R}_i^{6\times6}$ is a 6 × 6 matrix as described below, and $\tilde{O}_6$, $\tilde{1}_6$ are the null and identity matrices, respectively. In Eq. **S3**, ⊗ refers to direct product. The matrix $\tilde{R}_i^{6\times6}$ is given by

$$\tilde{R}_i^{6\times6} = -\begin{bmatrix} R_{Hxy}^i & \omega_H^i & 0 & \eta_{H,xy}^i & \pi J_{NH} & 0 \\ -\omega_H^i & R_{Hxy}^i & \omega_{1H} & -\pi J_{NH} & \eta_{H,xy}^i & 0 \\ 0 & -\omega_{1H} & R_{Hz}^i & 0 & 0 & \eta_{H,z}^i \\ \eta_{H,xy}^i & \pi J_{NH} & 0 & R_{2HxyNz}^i & \omega_H^i & 0 \\ -\pi J_{NH} & \eta_{H,xy}^i & 0 & -\omega_H^i & R_{2HxyNz}^i & \omega_{1H} \\ 0 & 0 & \eta_{H,z}^i & 0 & -\omega_{1H} & R_{2HzNz}^i \end{bmatrix}, \qquad \textbf{[S4]}$$

where i ε (G,E), $R_{Hxy}^i(=R_2^i)$, and R_{2HxyNz}^i are in-phase and anti-phase ^{1}H transverse relaxation rates, respectively, R_{Hz}^i is the ^{1}H longitudinal relaxation rate, R_{2HzNz}^i is the relaxation rate of longitudinal two spin order, ω_H^i is the ^{1}H chemical shift ($\Delta\omega_{GE} = \omega_H^E - \omega_H^G$, rad/s), ω_{1H} is the weak B_1 CEST field strength, J_{NH} is the one-bond ^{1}H-^{15}N scalar coupling constant, and $\eta_{H,xy}^i$ and $\eta_{H,z}^i$ are the transverse and longitudinal cross-correlated relaxation rates from ^{1}H-^{15}N dipole-dipole (DD)/^{1}H chemical shift anisotropy relaxation interactions (CSA). It is noteworthy that equilibrium ^{1}H magnetization is not included in the relaxation equations because the terms of interest at the start of the CEST delay are of the form $2I_zN_z$ and the phase cycle of the ^{15}N pulse before the t_1 period of the CEST scheme of Fig. 2*A* (ϕ_1) ensures that the small amount of H_z created during T_{EX} will cycle with ϕ_1 (see below). In contrast, terms proportional to equilibrium z-magnetization remain invariant and hence cancel due to the phase cycle.

During the fitting procedure $\eta_{H,xy}^i$ and $\eta_{H,z}^i$ values were set to 0 s^{-1} as simulations have established that the output p_E, k_{ex}, $\Delta\varpi$, and R_{Hxy}^i values were not affected when profiles generated with $\eta_{H,xy}^i$ (0–4.5) s^{-1} and $\eta_{H,z}^i$ (0–0.1) s^{-1} were fit to a model that assumed values of 0 s^{-1} for cross-correlation (see below). To simplify the fitting protocol, the relations $R_{Hz}^i = R_{2HzNz}^i - R_{Nz}^i$ and $R_{2HxyNz}^i = R_{Hxy}^i - R_{Nz}^i$ were used along with $R_{Hz}^G = R_{Hz}^E$, $R_{2HzNz}^G = R_{2HzNz}^E$. In principle, R_{Nz} values can be obtained from separate experiments and fixed in the fitting protocol; however, here we used R_{Nz} as a separate fitting parameter. Cross-relaxation with external protons was not considered explicitly in the fitting routine. Simulations (see below) show that the presence of an external proton 2.75 Å from the ^{1}H spin in question does not affect output PRE values, at least for the exchange parameters and overall molecular tumbling time (~4 ns) that are germane here. Because the t_1 evolution period in the scheme of Fig. 2*A* precedes the mixing period (T_{EX}) initial fractional populations of longitudinal order in ground and excited states, $2I_Z^GN_Z^G$, $2I_Z^EN_Z^E$ were set to $\pm p_G$ and 0, respectively, that is appropriate for the case where ^{15}N chemical shifts in these states are distinct. Ground and excited state R_{2HzNz} rates were assumed to be identical in the data fitting procedure, and simulations (below), as well as previous work (18, 44), establish the validity of this assumption.

Estimating errors in output values. Errors in extracted ^{1}H R_2 rates for spins in G and E were estimated from fits of CEST profiles using the covariance matrix method (61). Errors in populations and exchange rates were determined using a bootstrapping procedure (62), in which a series of datasets is generated, each of which contains 20 residues (those for which $|\Delta\varpi_{GE}| > \sim0.3$ ppm). For each residue there are four CEST profiles, one for each of the four experimental B_1 fields. For each bootstrapped dataset (2,475 and 3,848 for reduced and oxidized samples, respectively), 20 residues were chosen randomly with replacement from the pool of 20 residues and the corresponding CEST profiles fit using Chemex, as described above. The narrow distribution of p_E and k_{ex} values (Fig. S4*A*) indicates that ^{1}H CEST data for hTRF1 can be well fit to a two-state exchange model.

Simulations.

Reduction of NOE dips using longitudinal order. As described in the text, we used an approach based on the exchange of longitudinal order, $2I_zN_z$, to minimize the intensities of NOE dips that complicate analysis of ^{1}H CEST profiles. In the case of ^{1}H CEST experiments where exchange of longitudinal magnetization is monitored during a mixing period (corresponding to T_{EX} in Fig. 2*A*) that precedes t_1 evolution, we have previously shown that large NOE dips can be obtained because irradiation at the resonance frequency of spin S affects the intensity of a cross-peak derived from spin I due to a dipolar exchange mechanism (NOE) that couples I and S [see for example Fig. 1 of Bouvignies and Kay (33)]. In principle, there are a number of possible scenarios that could lead to NOE dips even in the case of profiles recorded using longitudinal order. As described below, this will occur when there are magnetization transfer pathways that connect spins I and S, so that irradiation at the frequency of spin S is transferred to spin I. However, in the longitudinal order case, terms that involve spin S, such as $2S_zN_z$, are not populated at the start of the CEST element, and this leads to a significant reduction in the intensities of the undesired dips. The transfer pathways that are germane here include the following:

i) $2I_zN_z \overset{NOE}{\longleftrightarrow} 2S_zN_z$, where ^{1}H spins I and S are proximal.

ii) $2I_zN_z \overset{\text{cross correlation}}{\longleftrightarrow} I_z \overset{NOE}{\longleftrightarrow} S_Z$.
In this scenario, longitudinal order $2I_zN_z$ evolves into I_z via ^{1}H-^{15}N dipolar/^{1}H CSA cross-correlation (Eq. **S4**) and I_z in turn cross-relaxes with proximal spin S. Irradiation at the frequency of spin S leads to a perturbation that can be transferred back to $2I_zN_z$. As expected, simulations establish this pathway to be unimportant as longitudinal dipolar/CSA cross-correlation scales as $J(\omega_H)$, where $J(\omega_H)$ is a spectral density function evaluated at the ^{1}H Larmor frequency (see below; $\eta_{H,z} \leq 0.1$ s^{-1} for the hTRF1 system considered here).

iii) $2I_zN_z \overset{B_1}{\longleftrightarrow} 2I_xN_z \overset{J_{NH}}{\longleftrightarrow} I_y \overset{B_1}{\longleftrightarrow} I_z \overset{NOE}{\longleftrightarrow} S_z$
Here B_1 and J_{NH} over the arrows denote the mechanism by which each of the terms is created.

We evaluated how large such effects can be by considering a set of simulations with k_{ex} = 150 s^{-1}, p_E = 13%, and including ^{1}H-^{15}N dipolar/^{1}H CSA cross-correlation ($\eta^i_{H,xy}$= 4.5 s^{-1}, $\eta^i_{H,z}$ = 0.1 s^{-1}) and cross-relaxation with an addition ^{1}H spin (S) at a distance of 2.75 Å from the proton spin of interest (Fig. S1). Note that 2.75 Å is the median of the minimum $^1H^N$-$^1H^N$ distance distribution in the native state of hTRF1.

The effect of cross-relaxation between S and I can be evaluated from the relations

$$\frac{d(2I_zN_z)}{dt} = -\rho(2I_zN_z) - \sigma(2S_zN_z),$$
$$\frac{d(2S_zN_z)}{dt} = -\rho(2S_zN_z) - \sigma(2I_zN_z), \quad \textbf{[S5]}$$

where (as described above) $2I_zN_z$ is the longitudinal order term of interest at the start of the CEST relaxation period (Fig. 2*A*), and we assumed that the autorelaxation rates of both longitudinal order terms, $2I_zN_z$ and $2S_zN_z$, are identical. It is worth noting that there is no magnetization of the form $2S_zN_z$ at the start of the T_{EX} duration because spins S and N are not scalar coupled.

We included cross-relaxation that interconverts I_z and S_z, according to

$$\frac{dI_z}{dt} = -\rho I_z - \sigma S_z,$$
$$\frac{dS_z}{dt} = -\rho S_z - \sigma I_z, \quad \textbf{[S6]}$$

although it is expected that this effect will be small because (*i*) initially only longitudinal order is present and (*ii*) relatively small values of T_{EX} are used. In Eqs. **S5** and **S6**, the autorelaxation rates, ρ, are defined as

$$\rho = \rho_{intra} + \rho_{ext},$$
$$\rho_{ext} = \left(\frac{\mu_0\hbar\gamma_H^2}{8\pi r_{HH}^3}\right)^2 [J(0) + 3J(\omega_H) + 6J(2\omega_H)], \quad \textbf{[S7]}$$

where ρ_{intra} includes all contributions to ρ with the exception of *I*-*S* ^{1}H-^{1}H dipolar relaxation (ρ_{ext}), γ_H is the gyromagnetic ratio of the ^{1}H spin, r_{HH} is the distance between protons S and I, μ_0 is the permeability of free space, and $\hbar = h/2\pi$ where h is Planck's constant. The spectral density function $J(\omega)$ is defined as

$$J(\omega) = \frac{2}{5}\frac{\tau_C}{1 + (\omega\tau_C)^2}, \quad \textbf{[S8]}$$

with τ_C the overall molecular tumbling time. Finally, the cross-relaxation rate constant, σ, is defined as follows:

$$\sigma = \left(\frac{\mu_0\hbar\gamma_H^2}{8\pi r_{HH}^3}\right)^2 [-J(0) + 6J(2\omega_H)]. \quad \textbf{[S9]}$$

For r_{HH} = 2.75 Å and $\tau_C \sim$ 4 ns, the cross-relaxation rate is −0.5 s^{-1}. In all calculations, we assumed that contributions from external spins are identical in both G and E for simplicity, although we recognize that in general this need not be the case.

Simulations were carried out using an extended basis set comprising 12 operators that includes the 6 listed in $\vec{M}$ above and an additional 6 where each I term is substituted by S. Values of σ were varied corresponding to tumbling times ranging from 4 to 24 ns.

Longitudinal order ($2I_zN_z$) and longitudinal magnetization (I_z)-based CEST profiles are plotted in Fig. S1 *A* and *B*, respectively. It is clear that, although the size of the NOE dips are significantly smaller for longitudinal order-based CEST, they are not completely eliminated in the case of slow tumbling times (larger proteins) or for long mixing times. The plots shown in Fig. S1*A* do not change if ^{1}H-^{15}N dipolar/^{1}H CSA cross-correlation rates are set to 0, establishing that the primary source of the NOE dip is the direct conversion of $2I_zN_z$ to $2S_zN_z$.

Estimating the effects of cross-relaxation with nearby protons. Contributions to the relaxation of the amide spin of interest (I) from proximal ^{1}H spins (S) are not taken into account in the relaxation equations used to fit the CEST data (Eqs. **S2–S4**). A rigorous inclusion of additional proton spins significantly complicates data analysis. In addition to increasing the basis set required to calculate the CEST profile ($\vec{M}$ of Eq. **S2**), an accurate description of the motion of the spins would also be required. It is expected that contributions to transverse relaxation rates from external spins would subtract out in the calculation of PREs (because they would be the same in both oxidized and reduced samples), and simulations described in the previous section establish that for a protein of the size of hTRF1, NOE dips are not visible in the $2I_zN_z$-based CEST profiles. However, we were particularly interested in evaluating how cross-relaxation involving proximal spins might influence extracted relaxation rates. Thus, simulations have been performed that include a single proton (S) placed at a distance of 2.75 Å from the proton of interest (I).

^{1}H CEST profiles were simulated as described above with σ = −0.5 s^{-1} (a value calculated for hTRF1), R_2^G = 31.25 s^{-1} and R_2^E = 51.25 or 181.25 s^{-1} that are typical for the reduced and oxidized samples studied here (k_{ex} = 150 s^{-1}, p_E = 13%, $\Delta\varpi_{GE}$ = 1.3 ppm). Subsequent fits of the data to a two-state model as described for the experimental profiles showed that there is little effect from neglecting cross-relaxation in the fitting procedure. For example, the fit values for R_2^G(R_2^E) are 30.7 ± 0.3 (49 ± 3) and 30.8 ± 0.3 s^{-1}(181 ± 3 s^{-1}) for input R_2^E = 51.25 and 181.25 s^{-1}, respectively, that compare very favorably with the input values.

Determining the robustness of extracted ground and excited state R_2 values from ^{1}H CEST. Ten ^{1}H CEST profiles, each at a pair of B_1 fields (25 and 50 Hz), were calculated using Eqs. **S2–S4** above, along with exchange parameters that are similar to those obtained from experiments on hTRF1 samples (k_{ex} = 150 s^{-1}, p_E = 13%). The cross-correlation rates, $\eta^i_{H,xy}$ and $\eta^i_{H,z}$, were set to 0 s^{-1}, and J_{NH} was fixed at −93 Hz in all simulations. All other parameters were residue specific and were varied between the ranges determined from the fitted experimental ^{1}H CEST profiles (and for R^G_{Nz} from ^{15}N CEST profiles, see below) of oxidized hTRF1 as follows: $\Delta\varpi_{GE}$: (−1.3,1.4) ppm, R^G_{Hxy} (15, 60): s^{-1}; R^G_{Nz}: (0.5, 3.5) s^{-1}; R^E_{Hxy}: (20, 200) s^{-1}; R^G_{2HzNz}: (4.5, 13) s^{-1}. Values of R^i_{Hz} and R^i_{2HxyNz} were calculated from $R^i_{Hz} = R^i_{2HzNz} - R^i_{Nz}$ and $R^i_{2HxyNz} = R^i_{Hxy} - R^i_{Nz}$, assuming identical longitudinal ^{1}H, ^{15}N, and two-spin order relaxation rates for nuclei in G and E. For each of the residue-specific parameters, 10 values were chosen within the specified range, and one value was assigned at random to each residue.

Each of the constructed CEST profiles was comprised of 82 (50) points over a 4-ppm range for a CEST B_1 field of 25 (50) Hz, with the spacing between points identical to that in the experiments. Data were generated for a spectrometer frequency of 14.0 T (600 MHz), T_{EX} = 125 ms. The noise floor of each of the simulated CEST profiles was determined based on the noise levels in the baselines of the experimentally derived CEST profiles for B_1 fields of 25 and 50 Hz (RMSDs range from 0.004 to 0.02 of the baseline I/I_o values). Ten RMSD values were picked for each B_1 field and assigned randomly to each of the 10 residues. Noise was added to each point of the CEST profile assuming a Gaussian distribution with mean 0 and SD equal to the noise RMSD value assigned to that particular residue. In this manner, 500 datasets were generated, and the simulated CEST profiles were then fit globally in the same way as the experimental data (see above) to extract thermodynamic, kinetic, and relaxation

parameters. Errors in the fitted values were calculated as 1 SD of the fitted parameters.

Input and fitted R_2^G and R_2^E rates correlate well with each other (Fig. S8 *A* and *B*), establishing that ^{1}H transverse relaxation rates of nuclei in both ground and excited states can be obtained reliably from ^{1}H CEST measurements. Small systematic deviations between the input and output values of R_2^G are very loosely inversely correlated to $\Delta\varpi_{GE}$ (Fig. S8 *D* and *E*), with larger $\Delta\varpi_{GE}$ values leading to more robust estimates of R_2^G, as would be expected due to the greater frequency separation between the ground and excited state dips.

Estimating the effects of cross-correlation between ^{1}H-^{15}N DD and ^{1}H CSA relaxation. As described above, $\eta^i_{H,xy}$ and $\eta^i_{H,z}$ rates were set to 0 s^{-1} in the Bloch–McConnell matrix (Eq. **S4**) used to fit the ^{1}H CEST profiles. To determine whether this leads to errors in the output p_E, k_{ex}, and R_2 values, we simulated CEST profiles (k_{ex} = 150 s^{-1}, p_E = 13%) with nonzero values of $\eta^i_{H,xy}$ and $\eta^i_{H,z}(\eta^G_{H,xy}=\eta^E_{H,xy};\eta^G_{H,z}=\eta^E_{H,z})$ and then fit them assuming a model where $\eta^i_{H,xy}$ and $\eta^i_{H,z}$ are set to 0, as has been done in the analysis of the experimental data. Values of $\eta^i_{H,xy}$ and $\eta^i_{H,z}$ rates (63) were calculated for a protein with an isotropic rotational correlation time of 4 ns (approximate value for hTRF1), assuming an axially symmetric ^{1}HCSA tensor with $(\sigma_\parallel - \sigma_\perp)$ values ranging from 5 to 15 ppm (64). The resulting $\eta^i_{H,xy}$ values (0–4.5 s^{-1}) are comparable to the range obtained experimentally by Bax et al. for a protein of similar size to hTRF1 (GB3) (65). A series of datasets comprising 10 ^{1}H CEST profiles at each of two B_1 fields (25 and 50 Hz) was simulated as described above, with a value of $\eta^i_{H,xy}$ and $\eta^i_{H,z}$ ranging from 0 to 4.5 s^{-1} and 0 to 0.1 s^{-1}, respectively, chosen for each residue. Profiles were globally fit as described for the experimental data.

The resulting p_E and k_{ex} values from the fits, 13.0 ± 0.1% and 150 ± 2 s^{-1}, are identical to the input values of 13% and 150 s^{-1}. Additionally, an excellent correlation between input and output values of R_2^G and R_2^E is obtained (Fig. S8 *F* and *G*) that does not change systematically with input $\eta^i_{H,xy}$ and $\eta^i_{H,z}$, confirming that setting $\eta^i_{H,xy}$ and $\eta^i_{H,z}$ to 0 in the fitting procedure has little influence on the output values of R_2^G and R_2^E for hTRF1.

Effect of differences in ground and excited state R_{2HzNz} values. R_{2HzNz} values of ground and excited state ^{15}N-^{1}H spin-pairs were assumed to be identical in both the experimental data fitting routine, as well as in the simulations described above. To test the validity of this assumption, we simulated ^{1}H CEST data for a single residue ($\Delta\varpi$ = 1.3 ppm) at two B_1 fields (25 and 50 Hz) as described above, using R^G_{2HzNz} = 10 s^{-1} and R^E_{2HzNz} ranging from 1 to 20 s^{-1}. To estimate PREs, residue-specific fits of the ^{1}H CEST over the two B_1 fields were carried out using a model that assumed identical ground and excited state R_{2HzNz} rates. Deviations in ground and excited state PREs from expected values were well within typical experimental errors, so that potential differences in R_{2HzNz} rates between exchanging states do not influence the extraction of PREs using the ^{1}H CEST approach, as least over the range examined here.

Resonance Assignments. Backbone resonance assignments of K52C hTRF1 were obtained from datasets recorded using a 1.2 mM ^{13}C/^{15}N sample dissolved in 50 mM Mes/50 mM KCl/1 mM NaN_3/7% (vol/vol) D_2O buffer, 35 °C, pH 6. A series of datasets including 2D ^{1}H-^{15}N HSQC, 3D HNCACB, and 3D CBCA(CO)NH (63, 66) were recorded (600 MHz). Assignments of urea-unfolded K52C hTRF1 were established using 2D ^{1}H-^{15}N HSQC, 3D HNCACB, 3D CBCA(CO)NH, 3D HN(CA)CO, 3D HNCO, and 3D HBHA(CO)NH spectra acquired at 600 MHz, 35 °C, on a 0.6-mM sample of ^{13}C/^{15}N K52C hTRF1 containing 3.5 M urea.

^{15}N CEST. ^{15}N CEST measurements on K52C-tempol hTRF1 were carried out to establish that addition of the tempol spin label to the K52C hTRF1 mutant does not change the nature of the excited state from what has been quantified previously for the WT protein (13). A previously published, pulse sequence has been used (18) along with a 440-μM ^{2}H/^{15}N sample of reduced K52C-tempol hTRF1. CEST B_1 field strengths were 17 and 34 Hz with 74 (17 Hz) and 38 (34 Hz) planes acquired, spanning a frequency range from 103.8 to 133.5 ppm. B_1 field strengths were calibrated as reported earlier (18). Intensities were extracted as described above for ^{1}H CEST data and fit to a two-state model of chemical exchange using the program Chemex to extract ^{15}N chemical shifts of the excited state (Fig. S9).

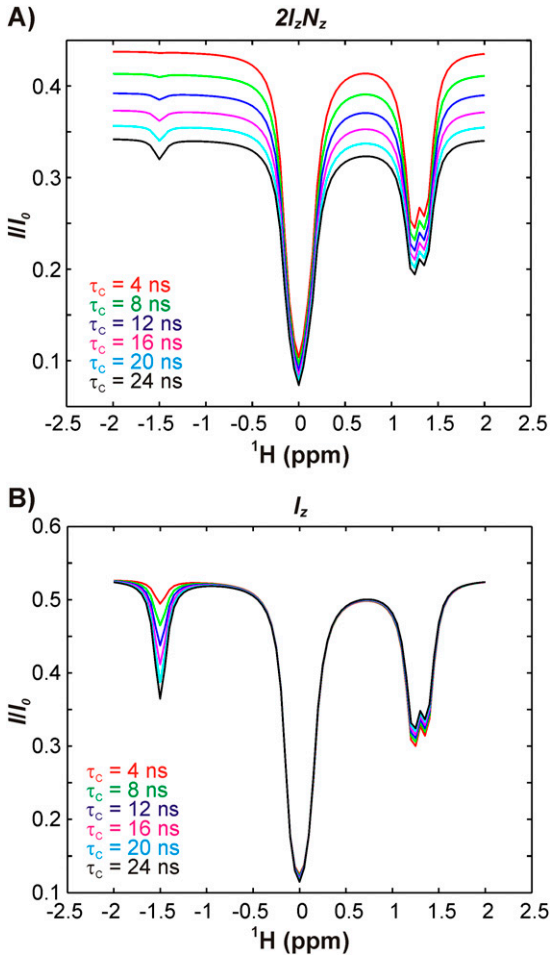

Fig. S1. Effect of cross-relaxation on CEST profiles acquired using longitudinal order, $2I_zN_z$ (*A*) and longitudinal magnetization, I_z (*B*). CEST profiles were simulated as described in *SI Text* including cross-correlated relaxation, with $\eta_{xy} = 4.5\ s^{-1}$ and $\eta_z = 0.1\ s^{-1}$. The ground (excited) state peak resonates at 0 (1.3) ppm, whereas the chemical shift of the proximal ^{1}H spin *S* is at −1.5 ppm (position of NOE dips). Cross-relaxation in the simulation originates from a single proton placed 2.75 Å away from the probe proton. Cross-relaxation values were determined for protein rotational correlation times varying from 4 to 24 ns and CEST profiles simulated for a B_1 field of 25 Hz and T_{EX} = 125 ms. Note that the simulations for I_z (*B*) assumed equilibrium values of longitudinal magnetization for spins *I* and *S* at the start of the CEST element, as would be expected for an experiment in which T_{EX} precedes t_1 or where ^{15}N chemical shifts of the one-bond coupled nitrogens are degenerate, for the case where the CEST delay follows t_1. Baselines in *A* decrease with increasing σ (or correlation time, τ_C) because the auto-relaxation rate of $2I_zN_z$ increases with correlation time: Eqs. **S5** and **S7**. In contrast, baselines do not change in *B* because the initial conditions include equilibrium values of both I_z and S_z (that are assumed to have equal relaxation rates). Thus, magnetization lost from *I* to *S* due to dipolar exchange is replenished exactly from magnetization gained from the transfer from *S* to *I*.

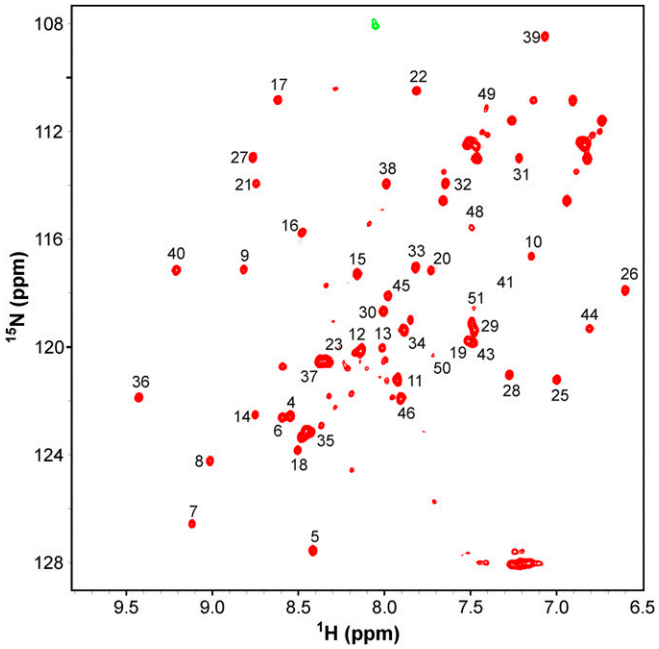

Fig. S2. ^{1}H-^{15}N HSQC spectrum of ^{2}H/^{15}N K52C-tempol hTRF1 with the nitroxide spin label in the reduced form, acquired at 600 MHz, 35 °C, pH 6. Resonance assignments are indicated alongside the peaks.

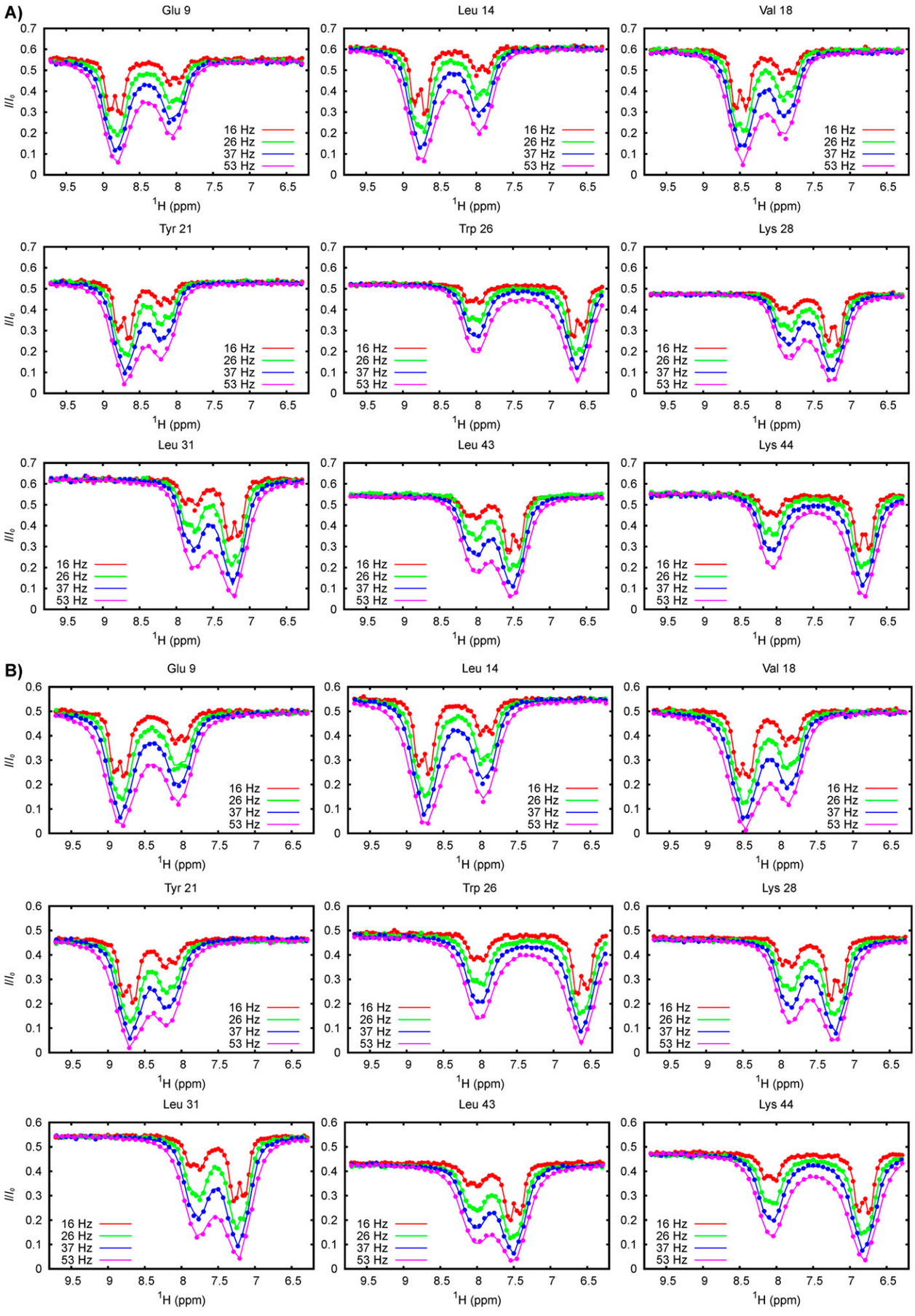

Fig. S3. ^{1}H CEST profiles for (*A*) reduced and (*B*) oxidized K52C-tempol hTRF1 acquired at four different B_1 field strengths using the pulse scheme of Fig. 2*A*.

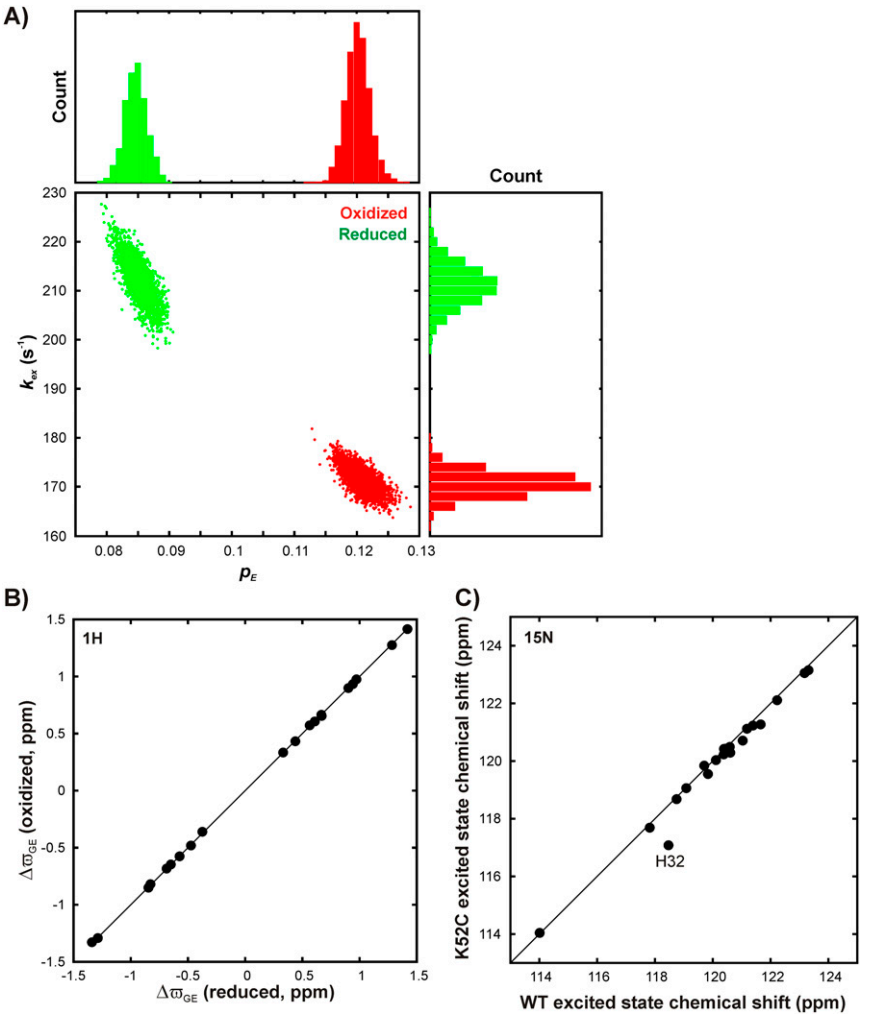

Fig. S4. (*A*) Populations of the excited state (p_E) and exchange rates (k_{ex}) for reduced (green) and oxidized (red) K52C-tempol hTRF1 obtained by bootstrapping fits of ^{1}H CEST data to a two-state model as described in *SI Text*. Differences in exchange parameters are likely due to slight differences in buffer conditions because it is known that the exchange parameters for hTRF1 are very sensitive to even slight variations in the composition of the buffer. (*B*) Differences between ground and excited state chemical shifts ($\Delta\varpi_{GE}$) correlate very well between oxidized and reduced samples showing that the excited states in both samples are identical. (*C*) ^{15}N chemical shifts of the excited state of WT hTRF1 (*x* axis) correlate well with the corresponding values for K52C-tempol hTRF1 (*y* axis). The solid line in *B* and *C* is $y = x$. The outlier corresponding to H32 may be the result of the differences in pHs of the two samples (K52C: pH 6; WT: pH 6.8).

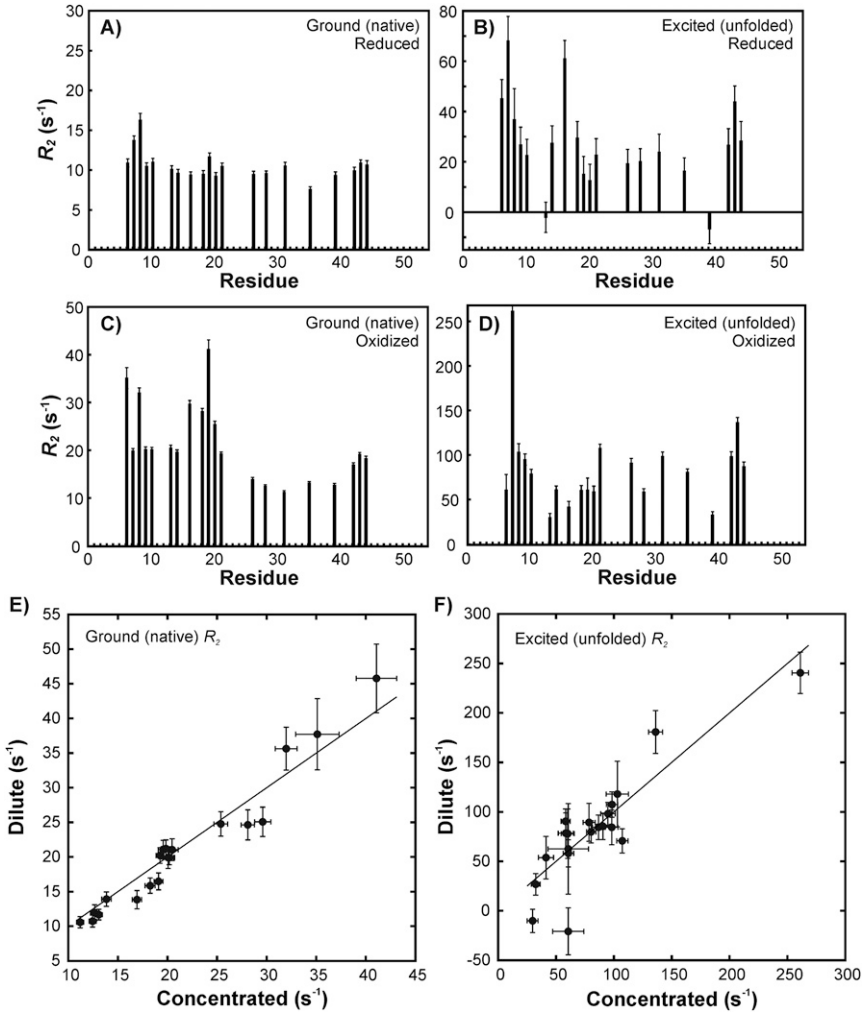

Fig. S5. Residue-specific ^{1}H R_2 values for ground (*A* and *C*) and excited (*B* and *D*) states of K52C-tempol hTRF1 in the reduced (*A* and *B*) and oxidized (*C* and *D*) forms of the spin label, derived from fitting ^{1}H CEST data globally to a two-state model of chemical exchange. (*E*) PREs measured in ground and (*F*) excited states of hTRF1 are independent of concentration. Correlation between R_2^G and R_2^E in concentrated (800 μM) and dilute (400 μM) hTRF1 obtained from ^{1}H CEST. The solid line in *E* and *F* is $y = x$.

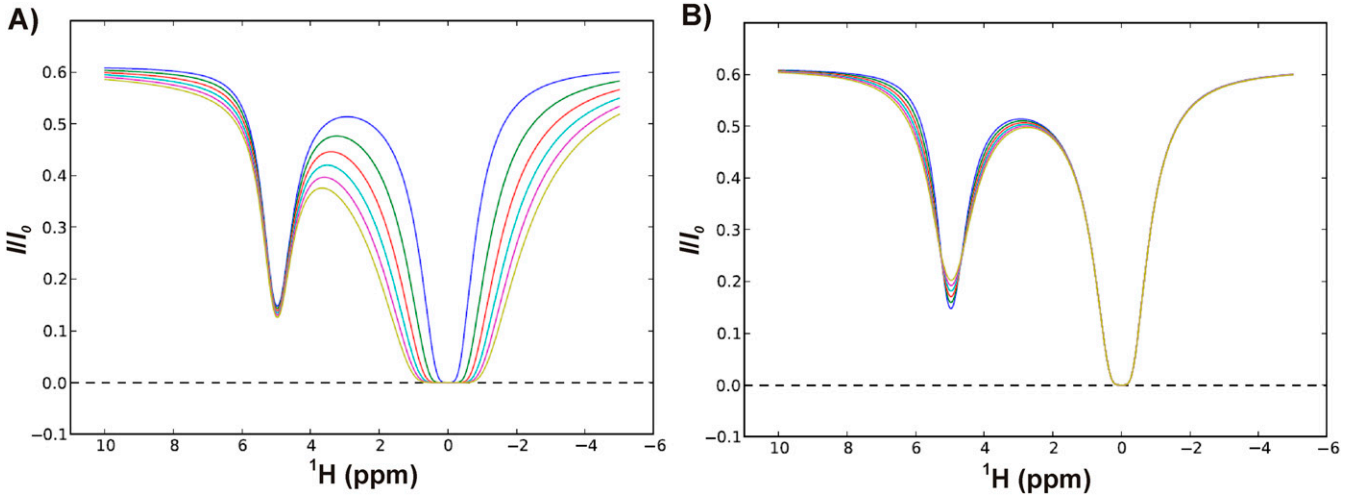

Fig. S6. Sensitivity of ground (*A*) and excited (*B*) state dips to changes in R_2^G and R_2^E, respectively. (*A*) R_2^G is varied from 0 (blue) to 100 (light green) s^{-1} keeping R_2^E constant (11 s^{-1}). (*B*) R_2^E is varied from 0 to 100 s^{-1} keeping R_2^G fixed at 11 s^{-1}.

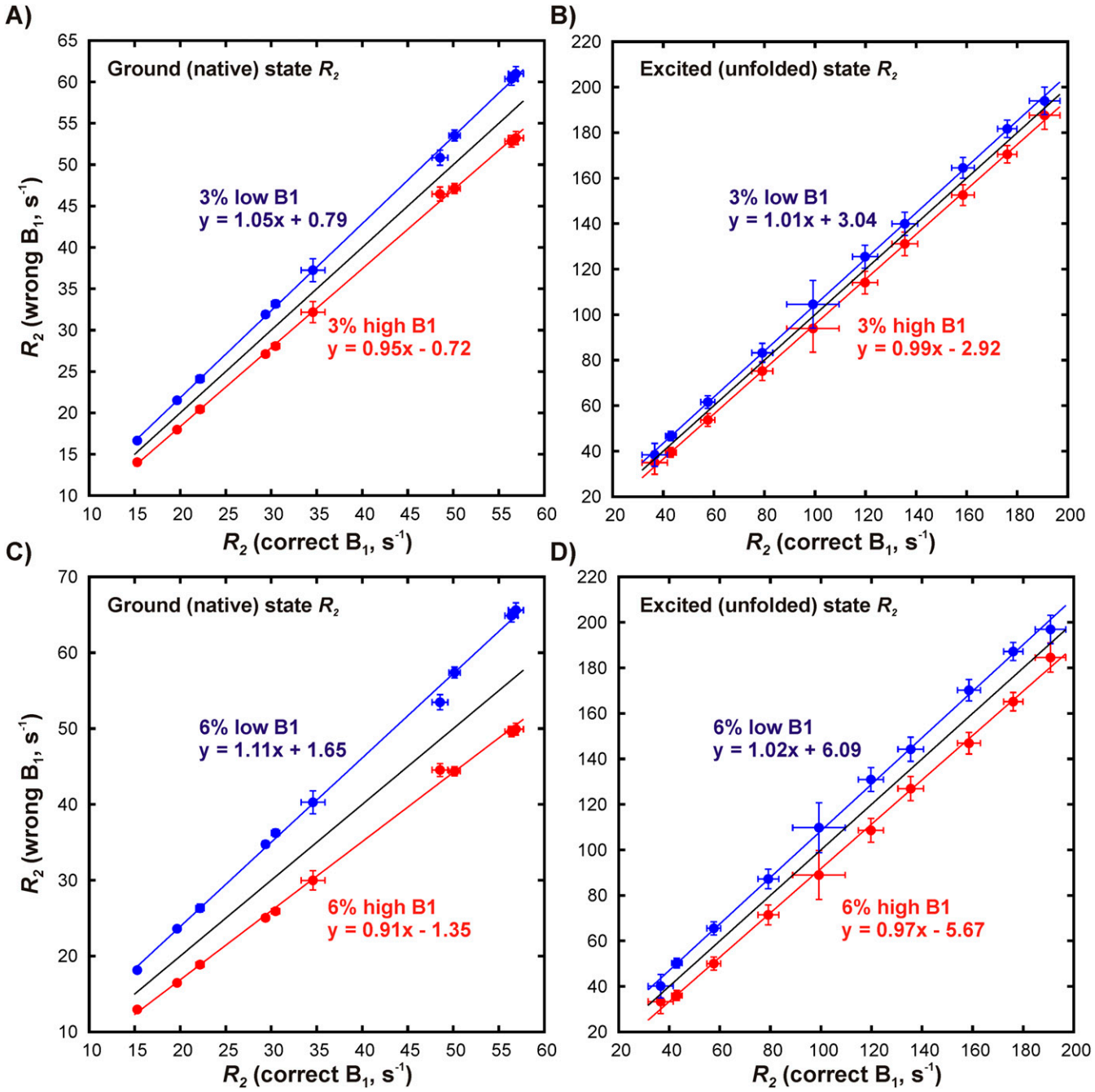

Fig. S7. Sensitivity of CEST-derived R_2^G and R_2^E rates to errors in B_1 calibration. (*A* and *C*) Ground and (*B* and *D*) excited state R_2 values obtained with correct B_1 in the fit (*x* axis) plotted against corresponding values on the *y* axis derived by missetting the B_1 field 3% higher (*A* and *B*; red), 3% lower (*A* and *B*; blue), 6% higher (*C* and *D*; red), or 6% lower (*C* and *D*; blue) than the correct value. The black line is $y = x$ in all panels, whereas colored lines are best fits of the data (circles) to a straight line whose equation is indicated.

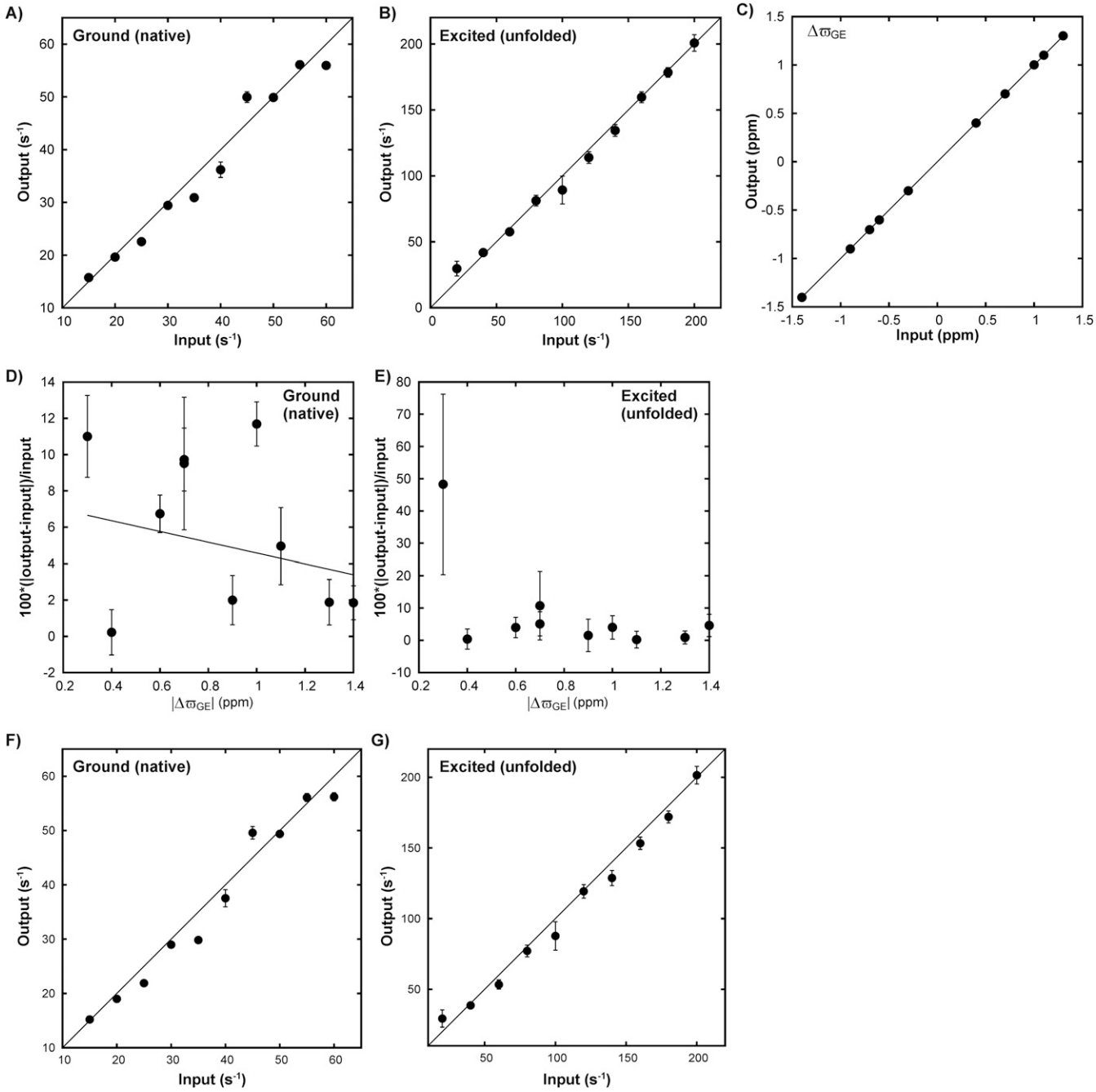

Fig. S8. (*A*) Ground and (*B*) excited state ^{1}H R_2 rates and (*C*) $\Delta\varpi_{GE}$ values obtained by fitting simulated ^{1}H CEST profiles correlate well with input values, showing that R_2 can be obtained robustly via ^{1}H CEST. Differences between ground state output and input R_2 values plotted as percentage of input rates show that the deviations in ^{1}H R_2 values roughly correlate inversely to $\Delta\varpi_{GE}$ (*D*). In *A*–*E*, the circles denote averages over the 500 simulations performed, and error bars are 1 SD from the mean. Correlation between input (*x* axis) and fit (*y* axis) values of R_2^G (*F*) and R_2^E (*G*) where data simulated using nonzero values of $\eta^i_{H,xy}$(from 0 to 4.5 s^{-1}) and $\eta^i_{H,z}$(0 to 0.1 s^{-1}) are fit to a model in which $\eta^i_{H,xy}$ and $\eta^i_{H,z}$ are fixed to 0.

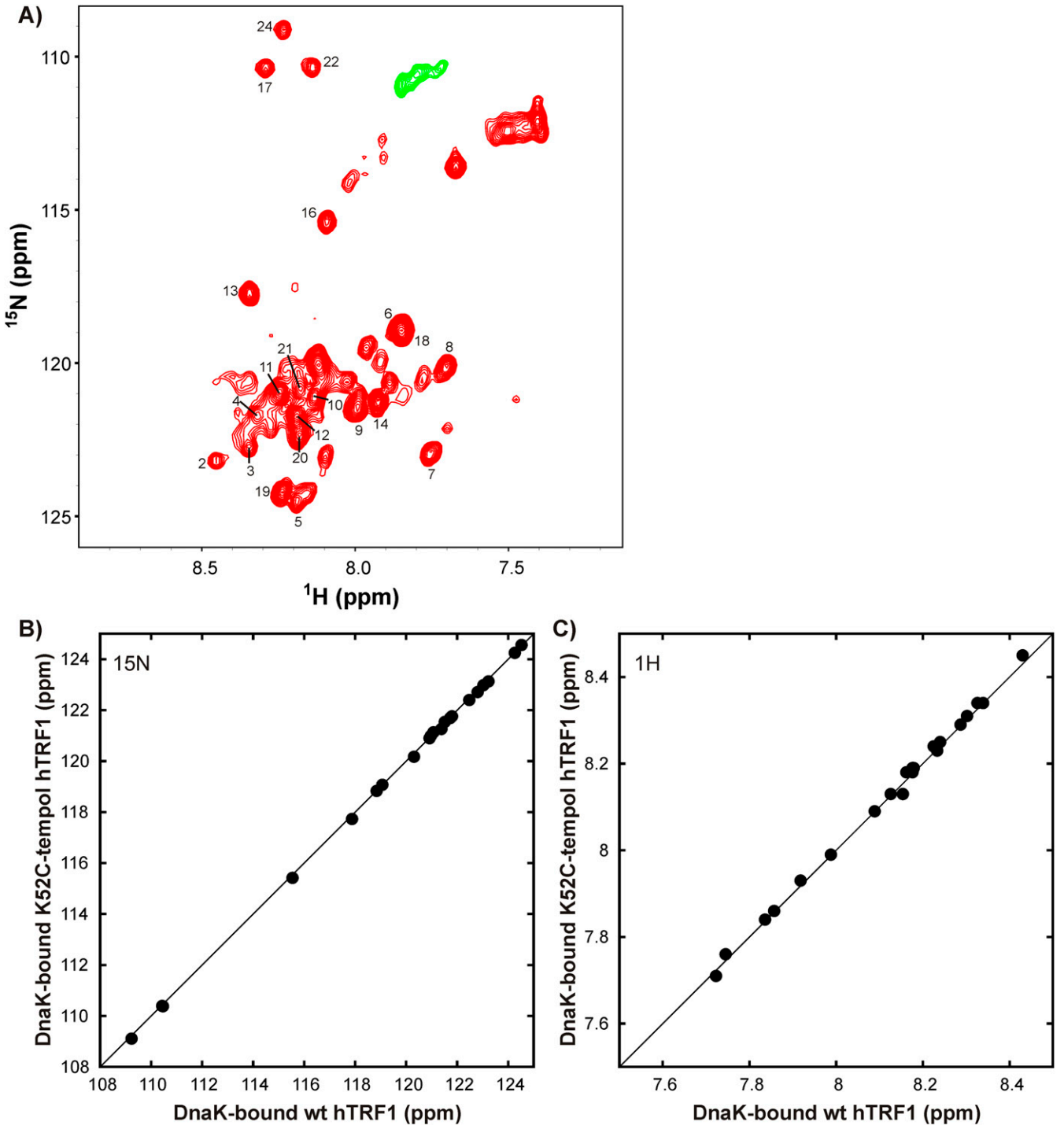

Fig. S9. The DnaK-bound conformations of WT and K52C-tempol hTRF1 are identical. (*A*) ^{1}H-^{15}N HSQC spectrum of 150 μM ^{2}H/^{15}N K52C-tempol hTRF1 with the nitroxide spin label in the reduced form, containing 300 μM ^{2}H ADP-DnaK, acquired at 600 MHz, 35 °C, pH 6. Resonance assignments are indicated alongside the peaks. Green-colored peaks are those that have been aliased in F_1. Comparison of ^{15}N (*B*) and ^{1}H (*C*) chemical shifts of ADP-DnaK–bound WT (13) and K52C-tempol hTRF1.

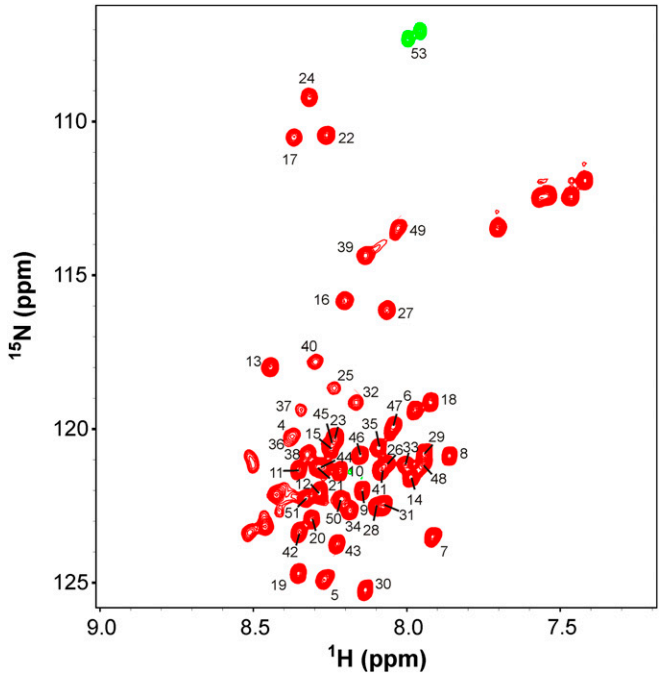

Fig. S10. ^{1}H-^{15}N HSQC spectrum of 670 μM ^{2}H/^{15}N K52C-tempol hTRF1 with the nitroxide spin label in the reduced form, unfolded in 3.5 M urea, acquired at 600 MHz, 35 °C, pH 6. Resonance assignments are indicated alongside the peaks. Green-colored peaks are those that have been aliased in F_1.